# Removal of Aqueous Phenol by Adsorption and Oxidation with Doped Hydrophobic Cryptomelane-Type Manganese Oxide (K−OMS-2) Nanofibers

**Boxun Hu, Chun-hu Chen, Samuel J. Frueh, Lei Jin, Raymond Joesten, and Steven L. Suib***

*Department of Chemistry, Unit 3060, 55 North Eagleville Road, University of Connecticut, Storrs, Connecticut 06269-3060*

*Received: January 27, 2010; Revised Manuscript Received: April 21, 2010*

Molecular adsorption and oxidation at manganese oxide/liquid interfaces has attracted increased interest due to its importance in the development of heterogeneous catalysts, microbial fuel cells, and selective adsorption materials. Here we report the adsorption and oxidation of phenolic compounds on $Cu^{2+}$, $Co^{3+}$, and $Ce^{4+}$ doped K−OMS-2 nanofibers. Different metal ion doped K−OMS-2 catalysts show distinct adsorption and oxidation ability. The structure and compositions of doped K−OMS-2 catalysts were characterized by X-ray diffraction and atomic absorption analyses. The relationships of catalyst structure-catalytic properties were discussed. The adsorbed polymeric nanospheres on doped K−OMS-2 nanofibers were investigated by field emission scanning electron microscopy, Fourier transform infared spectroscopy, transmission electron microscopy, and energy dispersive X-ray analyses. These nanospheres were totally oxidized to $CO_2$ in oxygen or air at 553−603 K catalyzed by doped and undoped K−OMS-2 itself. OMS-2 was regenerated with air or oxygen. The chemisorption and oxidation of phenol in an anaerobic environment ($N_2$) demonstrate that lattice oxygen of cryptomelane is involved in these processes. Free-radical mechanisms are proposed for the oxidation of phenol in $O_2$ and for the formation of phenolic nanospheres. Compared with undoped K−OMS-2, metal ion doped K−OMS-2 shows higher adsorption capacity of phenolic compounds and higher phenol removal rate.

## 1. Introduction

Molecular chemisorption at manganese oxide/liquid interfaces has attracted increased interest due to its importance in the development of heterogeneous catalysts,[1] microbial fuel cells,[2] and selective adsorption.[3] Recently, inexpensive manganese oxide based catalysts instead of noble metal catalysts have been investigated in the catalytic wet oxidation (CWO) of phenolic wastewater.[4,5] However, the adsorption of organic compounds on manganese oxide surfaces, which plays an important role in electron transfer and oxygen reduction, has not fully been explored. Phenol has attracted more attention in wastewater treatment because of its toxicity and wide occurrence in wastewater. Several conversion processes, currently under development for the production of synthetic fuel from coal, discharge substantial amounts of phenol (0.2−0.5 g/L).[6] Moreover, phenol is taken as a model compound for the study of adsorption and oxidation because phenol is an intermediate product in the oxidation of higher-molecular-weight aromatic compounds and phenol also converts to a series of intermediates on oxidation.[7]

Cryptomelane-type manganese oxide is an octahedral molecular sieve (OMS) composed of 2 × 2 edge-shared $MnO_6$ octahedral chains, which are corner shared to form one-dimensional tunnels (Figure 1). Potassium ions and water are located in the tunnels (designated K-OMS-2). Mixed-valent manganese ions ($Mn^{4+}$ and $Mn^{3+}$) are situated in the octahedral sites of cryptomelane. Transition metal ions (M) can be incorporated into the framework or tunnel sites.[8−10] Sizes and charges of M determine which sites are occupied. The synthetic counterpart of metal ion doped cryptomelane is known as octahedral molecular sieve M-K-OMS-2 ($M$ = doped metal ions). In recent years, some work has been published on the syntheses of cryptomelane-type manganese oxides[11−13] and their applications in the oxidation of benzene,[14] carbon monoxide,[15] and other hydrocarbons.[16] K-OMS-2 was found to possess excellent hydrophobicity and strong affinity for volatile organic compounds in the oxidation of benzene. Little has been reported on doping effects on the adsorption of substrates or on catalytic properties.

This research focuses on structure−property relationships for doped cryptomelane. These doped porous cryptomelane materials have high surface areas (40−100 $m^2/g$), more oxygen vacancies compared with undoped K-OMS-2, and more surface bonded OH groups. Porous M-K-OMS-2 nanofibers with diameters of 10−50 nm have attractive properties such as a large surface-to-volume ratio. The substitution of framework $Mn^{4+}$ with bivalent ($Cu^{2+}$) and trivalent ions ($Co^{3+}$) can create more oxygen vacancies to maintain an overall charge. Surface bonded OH groups on OMS-2 react with solute molecules and increase the adsorption of phenolic compounds. Solute molecules tend to attach to oxygen vacancies. Subsequently, electron and/or oxygen transfer between the metal oxide surfaces and solutes take place at these sites.[17]

Doped K-OMS-2 materials have dual roles in the removal of aqueous phenol, including adsorption and oxidation of phenol at moderate temperatures (298−423 K), pressures (80−150 psi), and pH (6−9). When phenol is adsorbed, phenol is oxidized to $CO_2$ and $H_2O$ in the catalytic wet oxidation with oxygen. The advantages of this process over microbial activated sludge processes[18] are that this process withstands high phenol loading rates and the fluctuations in phenol loading and does not produce any biological sludge. We show that the chemisorbed phenolic compounds on doped K-OMS-2 can reach up to 2−5 times the

* To whom correspondence should be addressed. E-mail: steven.suib@uconn.edu.

10.1021/jp100819a 
Published on Web 05/06/2010

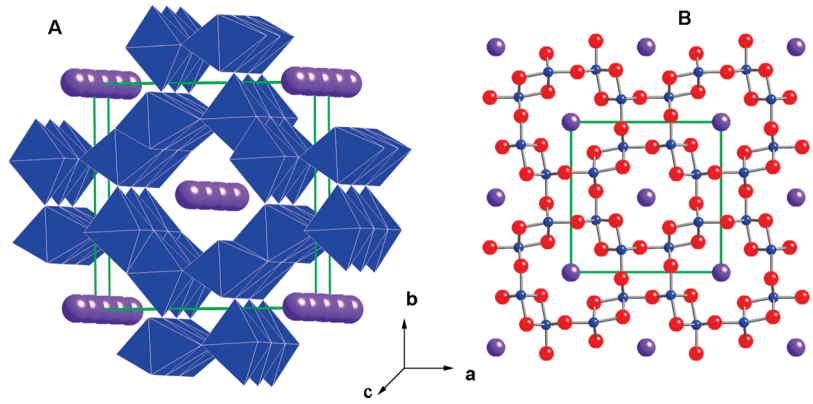


**Figure 1.** Polyhedral representation of K-OMS-2. The structure (A and B) is viewed down the *c* axis of a tetragonal unit-cell. The pink, blue, and red spheres represent K, Mn, and O, respectively.

weight of doped K-OMS-2. Compared with activated carbon (AC) adsorption,[19] phenolic compounds on K-OMS-2 can be oxidized by oxygen or air with the catalysis of doped K-OMS-2 at 573 K. The products are $CO_2$ and $H_2O$. Doped K-OMS-2 adsorbent and catalysts are regenerated.

The overall results in this research showed that doped M-K-OMS-2 catalysts had increased activity over that of undoped K-OMS-2 catalysts. Doped K-OMS-2 shows potential application in the removal of aqueous phenol. Structure activity relationships provide some scientific background for the development of highly efficient and low cost heterogeneous catalysts for applications in wastewater treatment.

## 2. Materials and Experimental Methods

**2.1. Catalysts Preparation.** Co−K−OMS-2 and Ce−K−OMS-2 were synthesized by hydrothermal methods. Complex cations oxidize $Mn^{2+}$ and doped porous M-K-OMS-2 nanofibers are self-assembled via a one-step hydrothermal synthesis. Cu−K−OMS-2 and K−OMS-2 were synthesized using a complex anion ($S_2O_8^{2-}$) to oxidize $Mn^{2+}$.

In a typical synthesis of Co−K−OMS-2, fresh $Co(OH)_3$ was prepared by the oxidation of $Co(NO_3)_2$ with NaClO in an NaOH solution. $Co(OH)_3$ was precipitated, centrifuged, and washed with deionized (DI) water three times. $Co(OH)_3$ (4.18 g), $MnSO_4$ (1.27 g), and $K_2SO_4$ (3.92 g) were mixed with 70 mL of $H_2O$ and 0.5 mL of concentrated $H_2SO_4$ solution (98.3%) in a 125 mL autoclave. The autoclave was heated in an oven at 473 K for 48 h. The slurry was washed with 1 L of DI water and dried in an oven at 473 K for 12 h. The syntheses of Cu−K−OMS-2 and Ce−K−OMS-2 followed the above procedures and conditions but use different recipes. $CuSO_4$ (0.69 g), $K_2S_2O_8$ (0.79 g), $MnSO_4$ (0.68 g), and $K_2SO_4$ (0.79 g) were mixed in 70 mL of $H_2O$ in a 125 mL autoclave. In the synthesis of Ce−K−OMS-2, $Ce(SO_4)_2$ (0.99 g), $MnSO_4$ (0.68 g), and $K_2SO_4$ (0.79 g) were mixed in 14 mL of $H_2O$ in a 23 mL autoclave. The synthesis of K-OMS-2 was described elsewhere.[20]

**2.2. Characterizations.** For the structural analysis of the adsorbents and catalysts, X-ray powder diffraction (XRD) was carried out with a Scintag XDS 2000 X-ray diffractometer equipped with a Cu Kα X-ray source ($\lambda = 1.54$ Å). The sample was ground to fine particles in an agate mortar. Fourier transform infared (FTIR) spectra were recorded on a Nicolet Magna 750 spectrometer in the range of 4000−400 $cm^{-1}$ with a resolution of 4 $cm^{-1}$ for samples in KBr (IR grade) pellets. These pellets were prepared by thoroughly mixing KBr with sample powder at a weight ratio of 50:1. KBr powder and samples were dried in a vacuum oven at 373 K for more than 2 h; the pellet sample was purged in pure $N_2$ for at least 15 min before FTIR was done.

For the morphology study, field emission scanning electron microscopy (FESEM) images were obtained using a Zeiss DSM 982 Gemini FESEM instrument with a Schottky emitter. The sample was suspended in ethanol and treated in an ultrasonic bath for 5 min and then dropped on Au and Pd sputter coated tips. Transmission electron microscopy (TEM) images were obtained using a JEOL 2010 FasTEM at accelerating voltages of 200 kV with an energy dispersive X-ray (EDX) analysis system. The samples were prepared by dispersing the material in 2-propanol. Then a drop of the dispersion was placed on a holey carbon coated copper grid and dried with an infrared lamp. Element analysis of adsorbed nanosphere/K-OMS-2 composites and Ce−K−OMS-2 was determined by EDX analysis. The composition of other doped K−OMS-2 materials was analyzed by atomic absorption (AA) analysis using a Perkin-Elmer 3110 AA spectrometer. Typically a sample of 20−80 mg was dissolved in 2−5 mL of concentrated HCL solution (36.5%) in a 50 mL Erlenmeyer flask. The flask was covered by a glass Petri dish with water on the top and heated to 353 K to digest the sample completely. The sample was dissolved after 2 h, and then the digested sample was diluted in a volumetric flask to an estimated concentration, which is between the low and high concentrations of the standard solutions.

Gas chromatography (GC) analyses were carried out with an SRI 8610C gas chromatograph with a flame ion detector and a thermal conductivity detector. Gas chromatography−mass spectrometry (GC−MS) analysis was conducted using a Hewlett-Packard GC (HP5890 series II) equipped with a mass-selective detector (MSD, HP5971 Series). A DB-17MS capillary polar column (20 m × 0.18 mm) was used in the temperature-programmed mode. The temperatures of the injector and GC−MSD interfaces were 543 and 553 K, respectively. The oven initial temperature was held at 308 K and then raised to 553 K at a rate of 10 K/min. The dwell time at 553 K was 4 min.

Temperature programmed oxidation−mass spectrometry (TPO−MS) analysis was done with a homemade setup. About 25 mg of the sample was placed in a quartz tube with a sintered glass fiber plugged on both ends. The quartz tube was purged with air (40 mL/min) and heated in a furnace with a programmable controller from 393 to 973 K at a ramp rate of 10 K/min. The outlet gas species were monitored with an MKS-UT1 PPT quadrupole mass spectrometer.

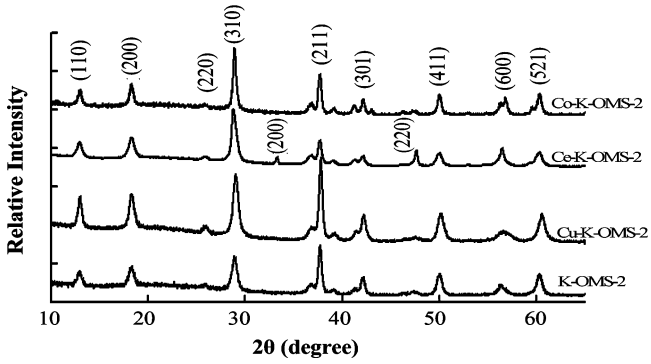


**Figure 2.** XRD patterns of doped and undoped K−OMS-2. Presence of $CeO_2$ impurities confirmed by 200 and 220 peaks for $CeO_2$ in the Ce−K−OMS-2 pattern.

Thermogravimetric (TGA) analysis was carried out on a Hi-Res TGA 2950 analyzer with a 60 mL/min air flow from room temperature to 523 K at a heating rate of 10 K/min, from 523 to 623 K at a heating rate of 3 K/min, and from 623 to 723 K at a heating rate of 10 K/min to control the oxidation rate of the used catalysts. For fresh catalysts, the heating rate was 10 K/min from room temperature to 973 K.

**2.3. Adsorption Experiments.** The adsorption of phenol at room temperature was analyzed by the TGA method. M−K−OMS-2 (40 mg) catalysts were added into a 40 mL of a phenol solution (5 g phenol/L) and stirred at room temperature for 0.5 h. Then the slurry was filtered and dried at 353 K for 12 h. The adsorption capacity was calculated from the weight loss from TGA analyses of the used catalysts.

In this work, the adsorption and oxidation of phenolic compounds was conducted at temperatures of 373 and 413 K. M−K−OMS-2 catalysts (40 mg) were added into 40 mL of a phenol solution (0.5−5 g phenol/L) in a 0.25 L Parr reactor with a magnetic stirrer (900 rpm). The chemisorption starts in pure $O_2$ at 100−150 psi in a closed system. After 2 h, the system was cooled to room temperature. Gases in the system were analyzed with a gas chromatograph. Catalysts were filtered from the slurry, and dried at 353 K for 12 h. Then they were characterized by TGA, XRD, FESEM, HRTEM, and TPO−MS. The filtered liquid was analyzed by GC−MS.

Adsorption in an $N_2$ (ultra high purity) environment was conducted with the above same conditions and at 100 psi. Before adsorption, the system was purged with $N_2$ until no $O_2$ was detected by GC analysis.

## 3. Results

**3.1. Structure and Composition of the Catalysts.** XRD was used to confirm the identity and phase purity of doped M−OMS-2 materials. $Cu^{2+}$, $Co^{3+}$, and $Ce^{4+}$ doped K−OMS-2 materials were synthesized at least three times following the preparation procedure (see section 2.1). All of the XRD patterns of the four different catalysts are shown in Figure 2. The XRD patterns of the catalysts from different batches are consistent with Figure 2. They can be indexed to a tetragonal phase of cryptomelane-type $MnO_2$ (JCPDS 29−1020). The average crystallite sizes of all of the OMS-2 materials (Table 1) calculated from the peaks of (110), (200), and (310) by the Scherrer equation[21] lie in the range of 19−25 nm. $Cu^{2+}$, $Co^{3+}$, and $Ce^{4+}$ doped K−OMS-2 materials have smaller average crystallite sizes than undoped K−OMS-2. Figure 3 of the Ce−K−OMS-2 sample shows the second phase of cubic $CeO_2$ is present in this sample. The (200) and (220) peaks of cubic $CeO_2$ (JCPDS 34−394) are clearly seen and the (111) peak overlaps the (310) peak of K−OMS-2 and shifts to a slightly lower $2\theta$. Typical FESEM images show that they are nanofibers with a length of 0.5−15 $\mu$m and a diameter of 15−25 nm. TEM confirmed that the nanoparticle size of these nanofibers is about 25 nm, which is consistent with the above crystallite size. The AA analysis shows that metal ions were doped into M−K−OMS-2 with different concentrations as shown in Table 1. K/Mn molar ratios of doped K−OMS-2 materials are 0.11−0.15. Cobalt ion doping leads to an increase in the concentration of $K^+$ in OMS-2.

**3.2. Adsorption and Oxidation of Phenol in Oxygen.** Table 2 shows the results of adsorption and oxidation of phenol with M−K−OMS-2. Co−K−OMS-2 and Ce−K−OMS-2 chemisorbed with about 3% of its weight of phenol at room temperature (RT) (Table 2). The adsorbed phenol at RT on Co−K−OMS-2 was oxidized at 583 K in air (Figure S1). K−OMS-2 has less chemisorption than that of doped K−OMS-2.

GC data show that the chemisorbed species are further oxidized and totally decomposed to $CO_2$ when the temperature increases. The total reaction is shown in eq 1.

$$C_6H_5OH\ (aq) + 7O_2\ (g) \rightarrow 6CO_2\ (g) + 3H_2O\ (l) \quad (1)$$

It is important to known how much phenol is adsorbed on catalysts and how much phenol is oxidized in $O_2$ by the catalysts. In this research, the adsorption data were obtained by TGA analysis of the postreaction catalysts. The total removal rate of phenol in the effluent, including both adsorption and oxidation, was obtained by GC−MS analyses of the liquid phase after the removal of catalysts by filtering. The deviations of TGA and GC−MS data were about ±2−5%. A very slow temperature ramp rate (2 K/min) was used in the TGA experiments to avoid sample spray due to strong oxidation. The adsorption and oxidation experiments for each catalyst were repeated at least two times.

A typical doped Co−K−OMS-2 catalyst was tested under identical reaction conditions: temperature = 373 K, oxygen $P$ = 150 psi, phenol concentration 0.6 g/L.[5,22] The weight ratio of $w_{cat}/w_{phen}$ was 2. The twice-averaged total phenol removal was 53 ± 2% in 1.1 h. Catalytic wet oxidation of phenol contributed 84 ± 2% of phenol conversion to $CO_2$. Low phenol concentration has less coverage of phenolic nanospheres on the catalyst and leads to a high percentage of phenol conversion to $CO_2$. Phenol adsorption on Co−K−OMS-2 was 64 ± 2 mg phenol/g catalyst, which was much less than 220 mg phenol/g catalyst of the well-crystallized Ce-incorporated OMS-2.[22] Substitution of K ions with Ce ions in the tunnel sites of OMS-2 increased the adsorption of phenol on the catalysts, and doped cobalt ions increased the phenol conversion to $CO_2$. The total phenol removal percentage with Co−K−OMS-2 catalysts increased 9% compared with the above-reported Ce-incorporated OMS-2 catalysts. But the total phenol remove percentage is still low because the regeneration of active oxygen species on catalyst surfaces is slow at low temperatures. The advantage of the catalytic wet oxidation technique is its capability of treatment of a relatively high concentration of phenol in wastewater at an intermediate temperature range.

To improve the catalytic oxidation effects of the catalysts, the reaction temperature was increased to 413 K and a low ratio of $w_{cat}/w_{phen}$ = 0.25 and a high concentration of phenol (5 g/L) were used. The twice-averaged values of the phenol adsorption and oxidation are reported in Table 2. The oxidation capacity is obtained by subtracting the adsorption capacity from the total

**TABLE 1: Catalyst Composition, Size, and BET Surface Area**

| | molar ratio | | | | |
|---|---|---|---|---|---|
| catalyst | K/Mn | M/Mn | surface area ($m^2/g$) | average crystallite size (nm) | micropore volume |
| K−OMS-2 | 0.12 | n.a. | 63 | 19.9 | 0.23 |
| Co−K−OMS-2 | 0.15 | 0.12 | 44 | 15.4 | 0.14 |
| Ce−K−OMS-2 | 0.11 | 0.01[a] | 60 | 13.2 | 0.18 |
| Cu−K−OMS-2 | 0.13 | 0.01 | 40 | 13.0 | 0.19 |

[a] Due to incomplete dissolution of the Ce−K−OMS-2 sample in cencentrated HCl, the molar ratio of Ce/Mn in Ce−K−OMS-2 was done by TEM-EDX. Other K/Mn and M/Mn ratios were done by AA analysis.

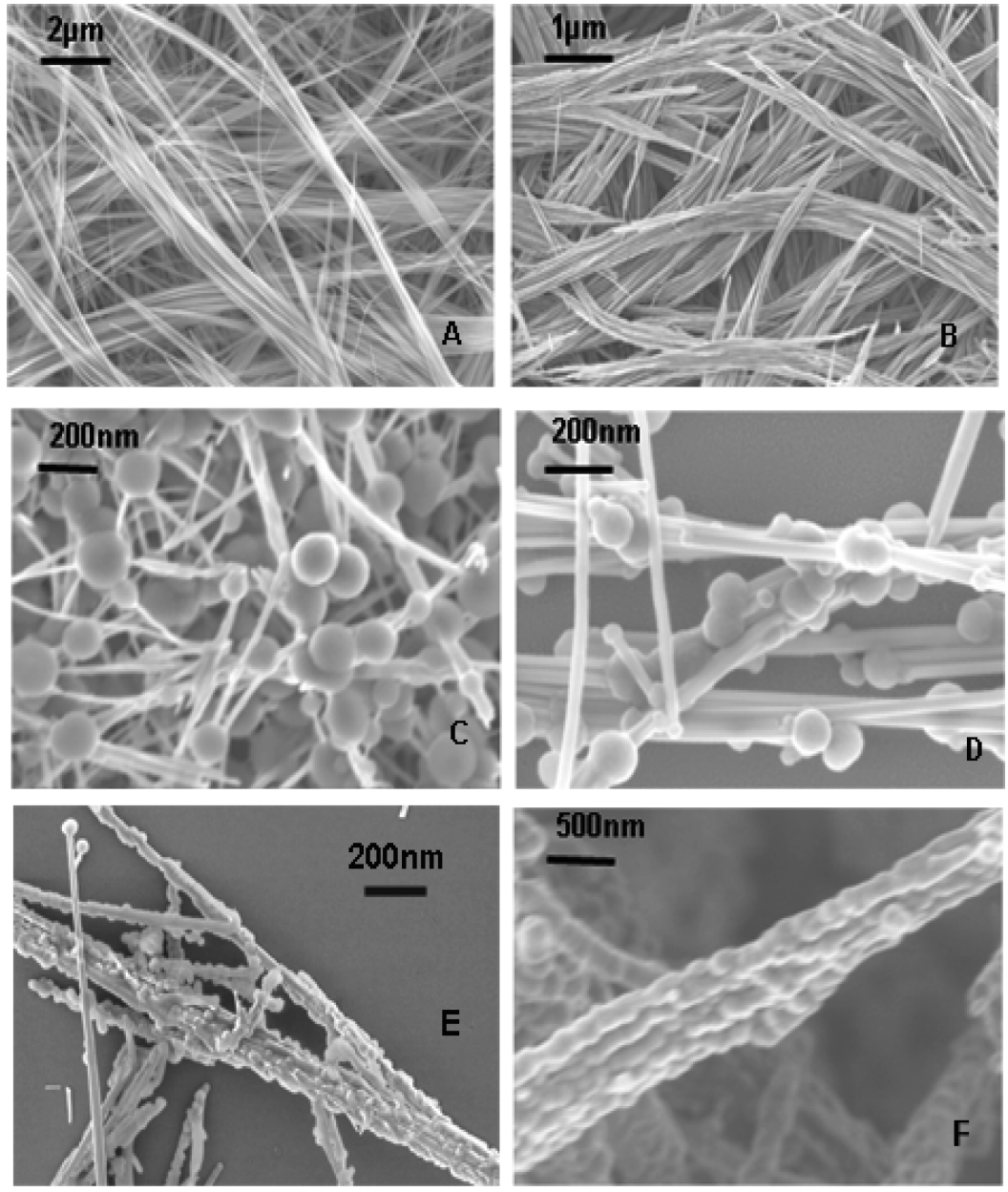


**Figure 3.** Typical FESEM images of OMS-2 catalysts. (A) Ce−K−OMS-2 before reaction, (B) regenerated Ce−K−OMS-2, (C−F) postreaction Cu−K−OMS-2, K−OMS-2, Co−K−OMS-2, and Ce−K−OMS-2 with organic nanospheres, respectively.

removal rate. Table 2 shows that doped K−OMS-2 materials have a higher phenol removal rate than undoped K−OMS-2. Co−K−OMS-2, Cu−K−OMS-2, and Ce−K−OMS-2 have 9.2, 6, and 5.25 times greater phenol removal rate than K−OMS-2, respectively.

**3.3. Morphologies and Compositions of Nanospheres.** The morphologies and compositions of postreaction catalysts were investigated by FESEM, TEM, and EDX techniques. FESEM images of fresh and postreaction M−K−OMS-2 are shown in Figure 3. FESEM images of postreaction samples show that the quantities and sizes of adsorbed nanospheres vary with doping ions ($Ce^{4+}$, $Co^{3+}$, and $Cu^{2+}$). The nanospheres of Cu−K−OMS-2 are larger than that of K−OMS-2. The adsorption of doped K−OMS-2 is more than that of undoped K−OMS-2. The FESEM data are consistent with TGA data of these postreaction catalysts. The chemisorption of phenol on

**TABLE 2: Results of Adsorption and Oxidation with Doped K-OMS-2 Catalysts[a]**

| | adsorption | | oxidation | total removal | |
|---|---|---|---|---|---|
| catalyst | 413 K | 298 K | 413 K | 413 K | phenol conversion, % |
| K-OMS-2 | 0.006 | 0.18 | 0.22 | 0.4 | 76.5 |
| Co−K−OMS-2 | 0.024 | 0.85 | 2.85 | 3.7 | 99.8 |
| Ce−K−OMS-2 | 0.017 | 0.47 | 1.63 | 2.1 | 98.9 |
| Cu−K−OMS-2 | 0.021 | 1.03 | 1.37 | 2.4 | 97.9 |

[a] Note: all the units are g phenol/h. g catalyst. Under the reaction conditions: Temp = 413 K, $C_{phenol}$ = 5.0 g/L, oxygen $P$ = 100 psi, and time = 2 h.

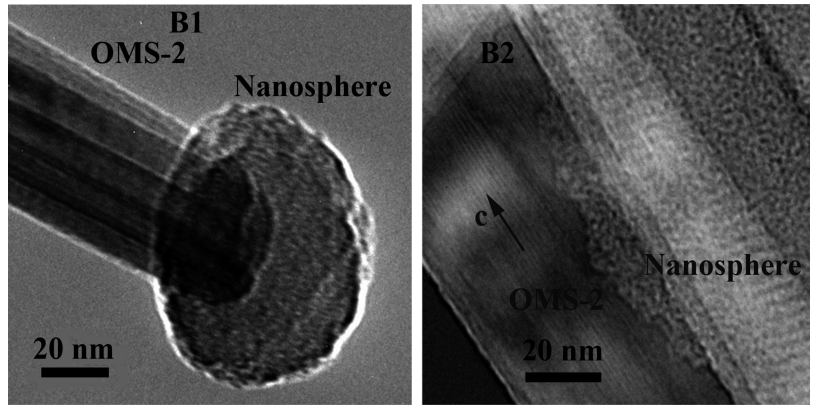


**Figure 4.** TEM images of adsorbed nanospheres. B1: nanosphere at end of K−OMS-2 tunnel, B2: nanosphere on the surface of K−OMS-2 nanofiber.

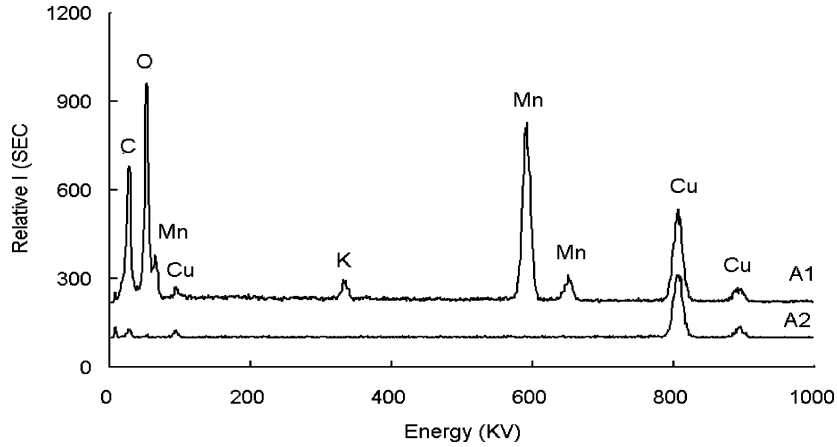


**Figure 5.** EDX spectra of K−OMS-2 nanofibers and adsorbed nanospheres. A1: a nanosphere and a nanofiber, A2: nanosphere only. The sample support contains Cu.

catalysts is generally considered to increase with temperature.[23] At room temperature, nanospheres do not form on the nanofibers. The nanospheres form at the end of fibers, then the nanospheres cover all the surfaces of the nanofibers at 423 K. The chemisorbed nanospheres on the end of M-K-OMS-2 nanofibers were not detached in ethanol solution under 10-min ultrasonic treatment (Figure 4, B1). These interesting phenomena will be discussed below in section 4.2.

Figure 4 (B1) shows that the radii of the adsorbed nanospheres are about 40 nm. The nanospheres formed at the tunnel openings of nanofibers imply that the tunnel openings of K−OMS-2 are reactive. Figure 4 (B2) shows the interface of K−OMS-2 and a nanosphere. The $c$ axis of K−OMS-2, the 2 × 2 tunnel direction, is parallel to the long axis of the fiber morphology (as labeled in Figure 4, B2). The nanospheres are chemisorbed on the K−OMS-2 surfaces. EDX spectra (Figure 5) at select areas reveal that the K-OMS-2 nanofiber with an adsorbed nanosphere is composed of K, Mn, C, and O, and the EDX spectra of the nanospheres show C and O peaks (H is not detectable by EDX). The formula of K−OMS-2 is $K_{0.12}MnO_2$. This indicates that the nanosphere is an organic nanosphere, and no manganese oxide is inside.

**3.4. FTIR Spectra of OMS-2/Nanospheres.** Phenol is not fully oxidized to $CO_2$, and part of the phenol molecules forms intermediates or polymeric species adsorbed on the catalysts during these oxidation processes.[24] Some of the intermediates, such as hydroquinone and *p*-benzoquinone, are more toxic than phenol.[25] Identifying and finally oxidizing them are the key points to evaluate the reduction of toxicity in the oxidation process.

To identify the adsorbed species on the M−K−OMS-2 nanofibers after the chemisorption of phenols, corresponding FTIR spectra were obtained and are presented in Figure 6. In Figure 6A, the absorptions at 721, 593, 525, and 471 $cm^{-1}$ can be assigned to the Mn−O vibrations of the $MnO_6$ octahedra in the framework of M−K−OMS-2. The broad band at 3340 $cm^{-1}$ is assigned to stretching of the bonded OH groups in the frameworks of Ce−K−OMS-2 and Co−K−OMS-2.[26] The band

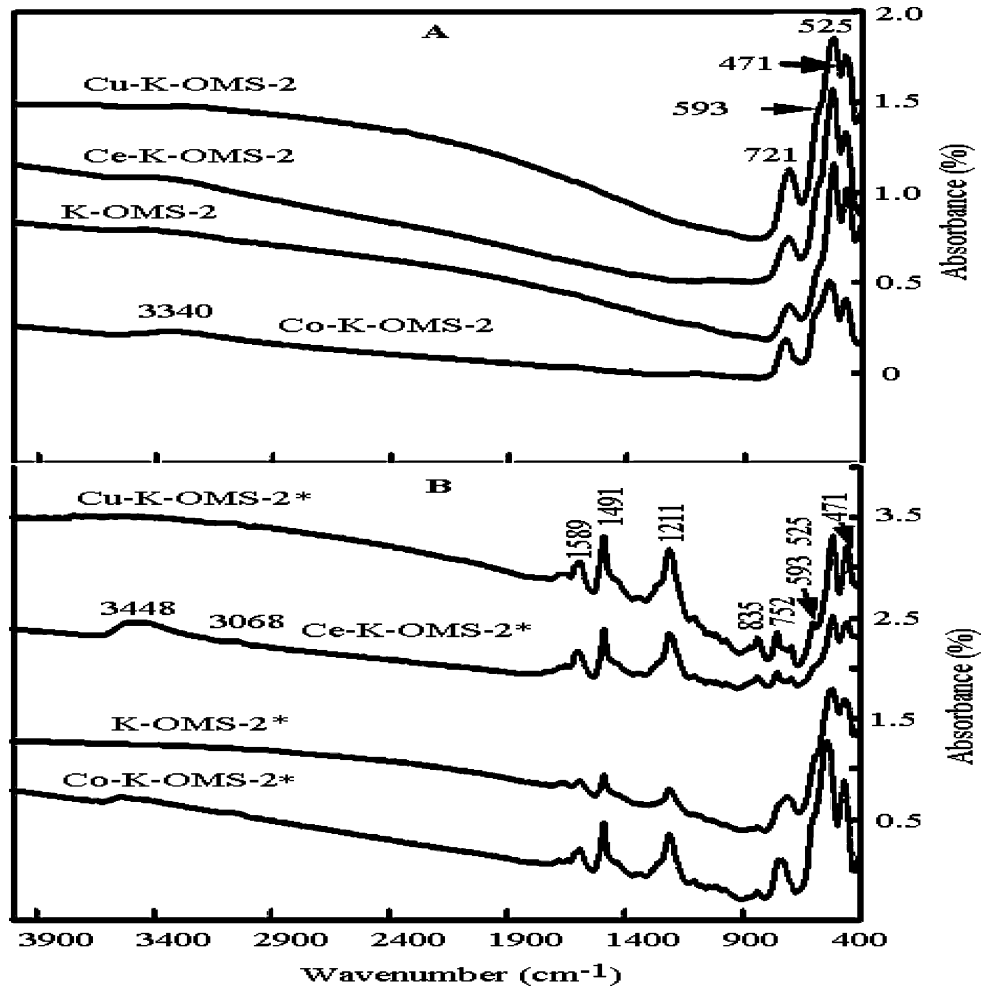


**Figure 6.** FTIR of M−K−OMS-2 before (A, top) and after (B, bottom) the adsorption of phenol. "*" represents the post reaction OMS-2 samples.

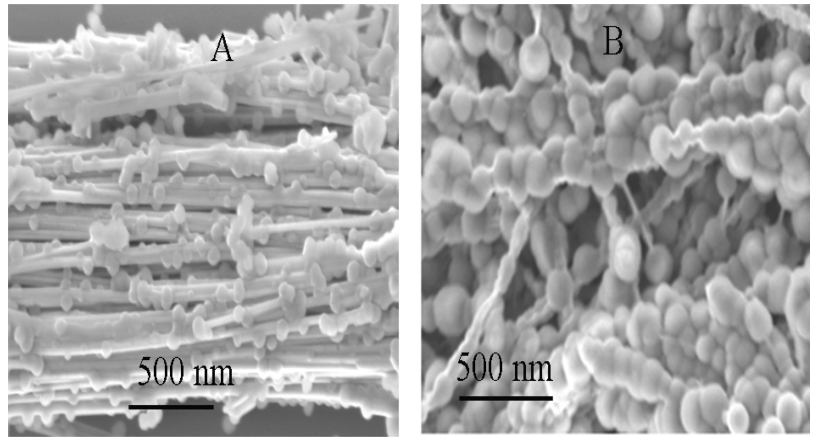


**Figure 7.** FESEM of adsorption of phenol on K−OMS-2 at 423 K. A: in $N_2$, B in $O_2$.

at about 1630 $cm^{-1}$, which is a bending vibration of the tunnel water species, is not observed here. In Figure 6B, the broad band at around 3448 $cm^{-1}$ can be attributed to characteristic hydrogen-bonded phenolic O−H vibrational bands and intramolecular hydrogen bonding between the repeating units in the polyphenol chains.[27] Two absorption bands at about 1589 and 1491 $cm^{-1}$ are due to the C═C vibrations of the aromatic ring. The broad vibrational band at around 1211 $cm^{-1}$ can be attributed to an overlapping C−O stretch of free phenolic −OH functional groups and the C−O−C stretch of phenyl ether. The band at 3068 $cm^{-1}$ belongs to the −C−H stretch of an aromatic ring. The bands at 835 and 752 $cm^{-1}$ belong to out-of-plane bending of ═C−H. There are still some phenolic −OH functional groups on the polyphenol.

**3.5. Adsorption and Oxidation in Nitrogen.** The role of lattice oxygen in OMS-2 is demonstrated in the chemisorption and oxidation of phenol in an anaerobic environment ($N_2$). FESEM images of Figure 7 show that there are still many organic nanospheres chemisorbed on OMS-2 nanofibers in $N_2$. The adsorbed nanospheres on OMS-2 are smaller and fewer in $N_2$ than in $O_2$. With the temperature increasing to 423 K, phenolic compounds gradually cover all of the surfaces of

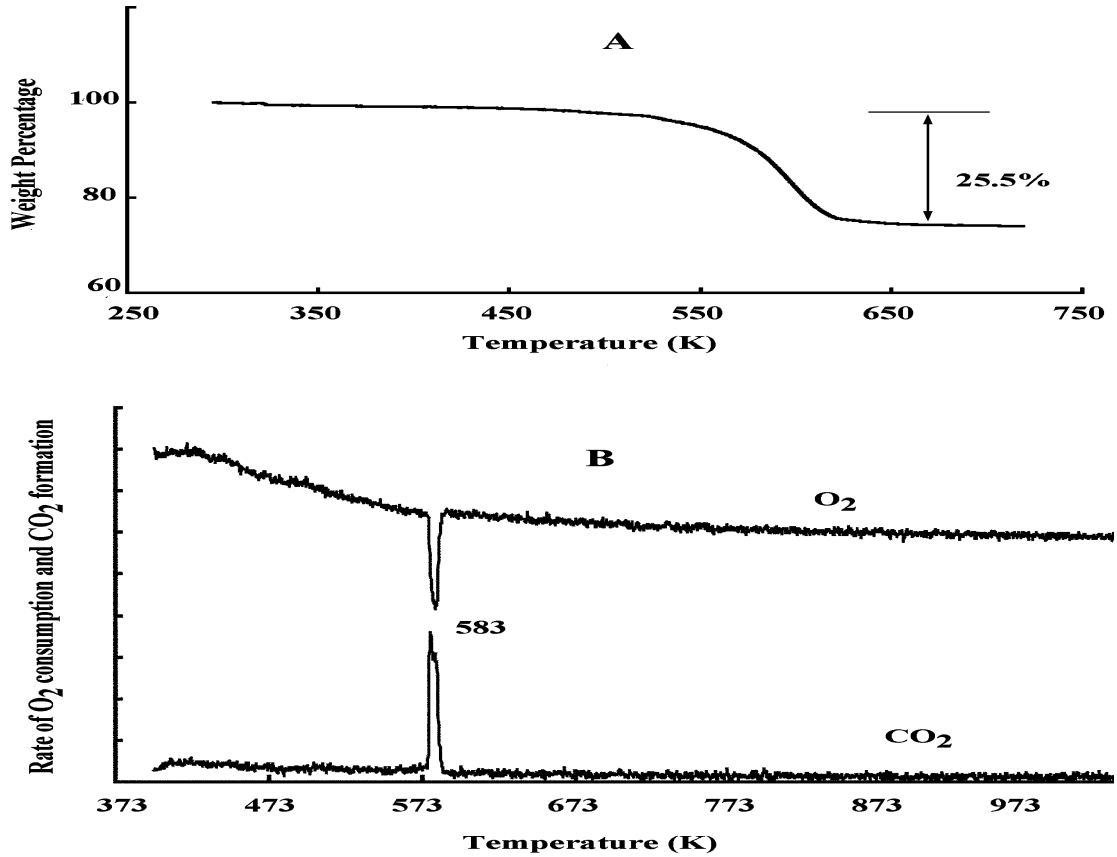


**Figure 8.** TGA (A) and TPO-MS (B) of K−OMS-2 adsorbed with phenolic compounds at 413 K.

nanofibers (Figure 7). This is consistent with TGA data of postreaction catalysts in $N_2$ and $O_2$. Figure 8 shows the adsorption peak of 1387 $cm^{-1}$ in $N_2$, which is assigned to −OH (phenol) deformation. This peak was not observed in Figure 6 of postreaction K−OMS-2 in $O_2$. This might indicate that the intermediate catechol formed in an $N_2$ environment and was not further oxidized without $O_2$.

**3.6. Regeneration.** Phenolic polymer covered the surfaces of the OMS-2 catalyst and therefore the catalyst gradually loses its activity. Regeneration of the catalyst is required. Figure 8 shows that the adsorbed phenolic polymer on the postreaction OMS-2 catalyst was totally oxidized in $O_2$ (or air) at temperatures as low as 583 K (eq 2).

$$HO-(C_6H_6O)_n-OH\,(s) + (3n + 1)O_2\,(g) \rightarrow 6nCO_2\,(g) + (3n + 2)H_2O\,(l) \quad (2)$$

In the above reaction, OMS-2 is a combustion catalyst. The oxidation reaction of organics on the OMS-2 surfaces is very strong and exothermic. The regeneration reaction of the postreaction Co−K−OMS-2 is strong and a weak flame can be seen in air. Therefore, diluted oxygen helps to control the temperature under 725 K and to retain the crystal structure of M−K−OMS-2 which is needed, because the cryptomelane structure will lose lattice oxygen at higher temperatures, and will be converted to bixbyite and lose part of its catalytic activity.[28] The FESEM image (Figure 3B) shows that the adsorbed phenolic polymer nanospheres on OMS-2 nanofibers were totally oxidized. Typical XRD patterns of regenerated Co−K−OMS-2 catalysts confirmed that the OMS-2 crystal structure is maintained (Figure S3). The stability of doped K−OMS-2 in combustion is important in practical applications, because many adsorbents and catalysts, such as activated carbon and supported catalysts, could be partially combusted at temperatures as low as 393 K.[29]

## 4. Discussion

**4.1. Doping Effect on Adsorption and Oxidation of Phenol.** M−K−OMS-2 doped with $Co^{3+}$, $Ce^{4+}$, and $Cu^{2+}$ have greater adsorption of phenol and higher catalytic activity than that of undoped K−OMS-2 (Table 2). These doped OMS-2 catalysts have high BET surface areas (40−63 $m^2/g$). High surface area generally increased the adsorption and activity. Other doping and structure factors described here showed greater effects on the adsorption and oxidation than surface area. Although XRD patterns reveal that $Co^{3+}$, $Ce^{4+}$, and $Cu^{2+}$ doped K−OMS-2 materials have the same 2 × 2 tunnel structure as K−OMS-2, the dopants make a distinct difference in the ability to adsorb and oxidize phenol. These metal ion dopants greatly enhance the adsorption properties and catalytic activities of the doped K−OMS-2 materials.

Considering the structures, the doped ions either locate in the framework to replace $Mn^{3+}$ and $Mn^{4+}$ or in the tunnel sites to replace $K^+$. In *a priori* incorporation of metal ions, Pauling's Rules suggest the crystal radius might determine whether the ion is doped into the framework or in the tunnel sites. Justified by the crystal radii (Table 3), $Co^{3+}$ would be in the framework positions of K−OMS-2 due to their almost equivalent ionic radii to those of the $Mn^{3+}$ ions. $Ce^{4+}$ ions were presumed to be in the tunnel positions of K−OMS-2 because of their much larger ionic radii compared to those of the $Mn^{3+}/Mn^{4+}$ ions. $Cu^{2+}$ ions may primarily be in the framework of K−OMS-2.

K−OMS-2 is a mixed-valent $MnO_2$ in which charge imbalance on the octahedral framework due to reduction of $^{VI}Mn^{4+}$ (VI and VIII represent the coordination numbers in the lattices)

**TABLE 3: Crystal Radii and the Ratio of Doped Ion Radii to Oxygen Ion[a30]**

| ions | $^{VI}Mn^{3+}$ | $^{VI}Mn^{4+}$ | $^{VI}Co^{3+}$ | $^{VIII}Ce^{4+}$ | $^{VI}Cu^{2+}$ | $^{VIII}K^{+}$ | $^{VI}O^{2-}$ |
|---|---|---|---|---|---|---|---|
| CR (Å) | 0.72 | 0.67 | 0.685 | 1.11 | 0.87 | 1.65 | 1.26 |
| $r_c/r_o$ | 0.57 | 0.53 | 0.54 | 0.88 | 0.69 | 1.31 | n.a. |

[a] Where CR is crystal radii and $r_c/r_o$ is the radii of cation divided by the radii of oxygen.

to $^{VI}Mn^{3+}$ is compensated by the presence of $^{VIII}K^{1+}$ in the tunnel site. This exchange, called "redox exchange" by Feng et al.[31] is shown in eq 3

$$^{VIII}\square^{\circ} + {}^{VI}Mn^{4+} \rightleftarrows {}^{VIII}K^{1+} + {}^{VI}Mn^{3+} \quad (3)$$

where $^{VIII}\square^{\circ}$ represents a vacant VIII-fold tunnel site (Figure 1). The formula of K−OMS-2 calculated from AA analysis (Table 1) with the assumption that the concentration of $^{VI}Mn^{3+}$ is related to that of $^{VIII}K^{1+}$ by the redox exchange (eq 3) is $K_{0.12}Mn_{0.88}^{4+}Mn_{0.12}^{3+}O_2$ and is consistent with occupancy of one-half of the available tunnel sites by $^{VIII}K^{1+}$. Charge compensation on the octahedral framework associated with doping of K−OMS-2 with $^{VI}Co^{3+}$ or $^{VI}Cu^{2+}$ can be described by similar redox exchanges

$$^{VIII}\square^{\circ} + {}^{VI}Mn^{4+} \rightleftarrows {}^{VIII}K^{1+} + {}^{VI}Co^{3+} \quad (4)$$

and

$$2^{VIII}\square^{\circ} + {}^{VI}Mn^{4+} \rightleftarrows 2^{VIII}K^{1+} + {}^{VI}Cu^{2+} \quad (5)$$

The formula of Co−K−OMS-2 calculated from AA analyses and using exchanges (3) and (4) is $K_{0.13}Mn_{0.87}^{4+}Mn_{0.02}^{3+}Co_{0.11}^{3+}O_2$, and that of Cu−K−OMS-2 calculated using exchanges (3) and (5) is $K_{0.12}Mn_{0.89}^{4+}Mn_{0.1}^{3+}Cu_{0.01}^{2+}O_2$. As with pure K−OMS-2, these formulas are consistent with half-occupancy of the tunnel site by $^{VIII}K^{1+}$.

Charge compensation associated with entry of $^{VIII}Ce^{4+}$ into the tunnel can be described by a redox exchange

$$^{VIII}\square^{\circ} + 4{}^{VI}Mn^{4+} \rightleftarrows {}^{VIII}Ce^{4+} + 4{}^{VI}Mn^{3+} \quad (6)$$

which can be coupled with exchange (3) to give the formula, $K_yCe_xMn_{1-4x-y}^{4+}Mn_{4x+y}^{3+}O_2$. If the tunnel site is half occupied, $x + y = 0.125$. The formula of Ce−K−OMS-2 calculated from TEM-EDX analysis (Table 1), assuming $^{VIII}Ce^{4+}$ occupies tunnel sites is $K_{0.11}Ce_{0.01}Mn_{0.85}^{4+}Mn_{0.15}^{3+}O_2$. Because our synthesis of Ce−K−OMS-2 produced excess cubic $CeO_2$ (Figure 2), we interpret this composition to represent the saturation limit for $^{VIII}Ce^{4+}$ in the K−OMS-2 structure. Single-phase Ce−K−OMS-2 (OMS-2 B) with the formula, $K_{0.09}Ce_{0.04}Mn_{0.76}^{4+}Mn_{0.24}^{3+}O_2$, has been produced by ion-exchange of K−OMS-2 with Ce (III) nitrate solution.[22] Attempts to introduce additional Ce into the structure produced a two-phase mixture with cubic $CeO_2$. Table 2 shows that the substitution of K ions with Ce ions showed the increase of phenol adsorption on the catalyst and also the increase of the catalytic activity of phenol conversion to $CO_2$.

**4.2. Possible Mechanism of Adsorption and Oxidation.** Covalently bound surface OH groups on Co−K−OMS-2 and Ce−K−OMS-2 show a broad band at 3340 $cm^{-1}$ (Figure 6 A). These covalently bound surface OH groups account for about 2% adsorption of phenol on Co−K−OMS-2 and Cu−K−OMS-2 at room temperature. At increased temperatures, more OH groups are produced from the hydroxylation of the surface oxides.[32] The hydroxylation reaction can be described by

$$M-O\ (s) + H_2O\ (l) \rightarrow M-OH\ (s) + -OH\ (aq) \quad (7)$$

Both covalently bound surface OH groups and OH groups produced by eq 7 react with phenol (Ar−OH) to form phenolic complexes via eqs 8 and 9

$$M-OH\ (s) + Ar-OH\ (aq) \rightarrow M-O-Ar\ (s) + H_2O\ (l) \quad (8)$$

$$M-OH_2^{+}\ (s) + Ar-OH\ (aq) \rightarrow M-O^{+}H-Ar\ (s) + H_2O\ (l) \quad (9)$$

M−OH represents the surface OH groups bonded to metal ions M. More M−OH species bind more phenol molecules. Considering that the hydroxylation reaction goes fast at an increased temperature, the adsorption of phenol is significant at high temperatures with high (40−64 $m^2/g$) surface area materials.

The free-radical mechanism is involved in the catalytic wet oxidation of phenol in oxygen. The one-electron oxidation of phenol by mixed valent $Mn^{4+}/Mn^{3+}$ ion in the doped K-OMS catalysts accounts for the formation of the phenoxy radicals (see reaction 10).[33] These phenoxy radicals not only are involved in the degradation of phenol but also cause the formation of the phenolic nanospheres due to coupling of phenoxy radicals and phenol. Gopalan et al.[34] reported the free radical chemistry of phenol oxidation in supercritical water in both gas and solution phases, and the formation of phenol dimerization products was due to phenoxy radical−radical recombination. In our catalytic wet oxidation of phenol, dimerization products were not detected in the liquid phase by GC−MS. However, dimerization reactions may proceed on the surface of the nanofiber catalysts. Phenolic nanospheres formed on the solid doped K−OMS-2 nanofibers. The functional groups of −Ar, Ar−O−Ar, and −OH shown in FTIR spectra of the postreaction catalysts suggested that phenoxy radical coupling accounts for the formation of phenolic nanospheres. To explain the formation of the phenolic nanospheres, Scheme 1 shows the typical reactions of the phenoxy radicals and phenol. Equation shows the isomerism of the phenoxy radicals. These phenoxy radicals have radical−radical reactions (see reaction 12) and radical-molecule reactions (see reaction 13). 2,2′-Biphenol dimers form poly(biphenol) on the catalyst surface, while 2-phenoxyphenol can terminate the polymerization process (the reactions are not shown here). The coupling and polymerization processes explain the formation of phenolic nanospheres although they could be more complicated than the reactions shown in Scheme 1.

Catalytic processes of phenol oxidation involve the Mars-van Krevelen mechanism[35] of oxidation at the interfaces of the catalyst surfaces and phenol molecules. Mixed valent $Mn^{4+}/Mn^{3+}$ ion are the active sites of the catalysts. Phenol was reported to adsorb exclusively on the metal ion sites at their higher oxidation states ($Mn^{4+}$),[36] and is oxidized by $Mn^{4+}$ ions and not directly by molecular oxygen in the gaseous phase. Lower oxidation state ions ($Mn^{3+}$) are reoxidized to $Mn^{4+}$ by adsorbed oxygen atoms when pH is controlled in the range of 6−9.[37] Leaching of $Mn^{2+}$ was not observed in the effluent by

**SCHEME 1: Formation of Phenoxy Radicals and Dimers**

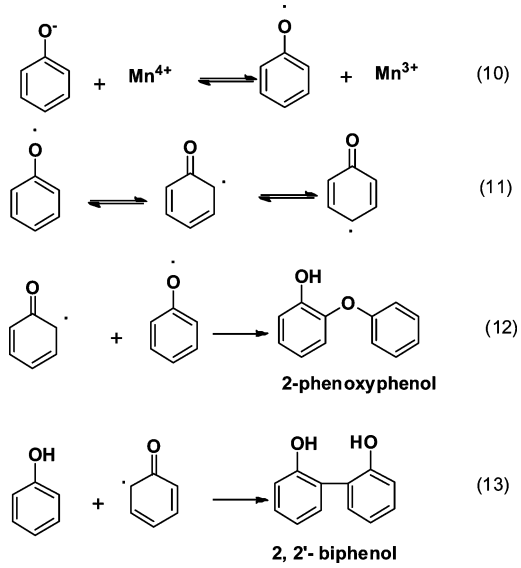


AA analyses under this pH condition. Gas phase oxygen provides OMS-2 catalysts with adsorbed oxygen species via a diffusion process.

The adsorption of phenol on adsorbents and catalysts is determined by surface area, pore size distribution, phenol concentration, and pH of the solution. When these parameters were kept the same, the effect of temperature on adsorption of phenol was observed in section 3.3. Phenol binding reactions 8−9 must overcome the entropic penalty (up to +15 kcal/mol) for the loss of rotational and translational degrees of freedom as two reactants combine to become one complex, and the penalty (about 0.6 kcal/mol) for restriction of bond rotation.[38] The phenol binding reactions are fast at elevated temperatures. Comparing the phenolic nanosphere density of FESEM images (Figure 3D and Figure 7B), the chemisorption of phenol at 423 K was more than that of 413 K. The phenol binding on doped K−OMS-2 nanofibers is favored at defect sites, such as oxygen vacancies.[39] The ends of tunnel sites of doped K−OMS-2 might have more defects leading to the formation of phenolic nanospheres.

Phenol oxidation needs to overcome an activation energy. Fast degradation of phenol takes place at temperatures between 403 and 423 K, at which temperatures industrial phenol wastewater is often discharged. To utilize the waste heat, doped K−OMS-2 catalysts are added into hot phenol wastewater in a high-pressure oxygen reactor with stirring for adsorption and oxidation. In the disposal of phenol from synthetic fuel plants, utilization of the industrial waste heat in this process is an effective way to save energy and to reduce the treatment cost.

The enhanced oxidation activity of doped K−OMS-2 catalysts at reaction temperatures (375−425 K) could be explained by the temperature programmed reduction (TPR) of doped K−OMS-2 with 5% CO/He (balance).[40] Co−K−OMS-2 and Cu−K−OMS-2 showed that CO was oxidized by oxygen species of OMS-2 between 340−400 K, which is the operating temperature range of phenol oxidation. In TPR experiments, active oxygen species were minimal and showed a weak peak because no fresh oxygen was supplied. But in the oxidation of phenol with oxygen, the depleted activate oxygen species of OMS-2 can be regenerated as reported by Yin et al.[41] via oxygen diffusion. Therefore, doped K−OMS-2 materials could be used as catalysts with enhanced catalytic activity. Increasing the reaction temperature could help regenerate the active oxygen species, and therefore improved the catalytic wet oxidation rate of phenol. This gives an explanation why Erena et al. and Abecassis-Wolfovich et al. observed that the removal of phenol at low temperatures is mainly attributed to the strong adsorption of phenolic compounds on solid catalysts, and why the catalytic wet oxidation is the main contribution (up to 77%) to the total phenol removal at a higher temperature with an almost 100% phenol removal efficiency in our experiments.

Further adsorption experiments were conducted in $N_2$ to compare with the results in $O_2$ to determine the role of oxygen in the adsorption and oxidation of phenol with mixed-valent OMS-2 catalysts. TGA analysis data show that the chemisorption of nanospheres on K−OMS-2 in $N_2$ is much less than the chemisorption in $O_2$ (only 38% adsorption in $O_2$). Only about 3 ppm $CO_2$ in the gas phase was detected by GC analysis. This is due to the lack of $O_2$ in the system. Reactive oxygen species, which are observed between 340−400 K in TPR experiments, were depleted in the oxidation of phenol but cannot continuously form from gas phase oxygen. The chemisorption of phenolic compounds in $N_2$ implies that reactive oxygen species in OMS-2 are directly involved in the oxidation.

## 5. Conclusions

Doped cryptomelane-type M−K−OMS-2 nanofibers were synthesized and tested as catalysts and adsorbents in the abatement of phenol in wastewater. TEM and FESEM images show novel nanospheres are adsorbed on the nanofibers of doped and undoped K−OMS-2 surfaces. EDX and FTIR analyses confirmed that the compositions of the nanospheres were pure organic phenolic compounds, such as poly(biphenol). The mechanism of the formation of the nanospheres is proposed. FTIR spectra of doped K−OMS-2 show bound OH groups. Surface OH groups on OMS-2 increase the adsorption of phenol. These OH groups form in the synthesis process by doping metal ions, and in the hydroxylation of OMS-2 at high temperatures (373−423 K). Nanospheres form during the oxidation of phenol to intermediate catechol.

Doping K−OMS-2 catalysts with $Ce^{4+}$, $Co^{3+}$, and $Cu^{2+}$ significantly increases the activity of doped M−K−OMS-2 in comparison to undoped K−OMS-2. The highest efficient catalyst tested here is Co−K−OMS-2 catalyst with a phenol removal rate of 3.7 kg phenol/h.kg catalyst. These catalysts have shown high catalytic activities and stability in heterogeneous reactions at moderate temperatures. These types of catalysts that can be used in liquid−solid, solid−solid, and gas−solid heterogeneous reactions are rare. Doped K-OMS-2 catalysts have larger adsorption capacity (1.03 g phenol/h.g Cu−K−OMS-2) of phenol than activated carbon (0.24 g phenol/5 days.g AC).[42] Doped K-OMS-2 is more stable in combustion and in regeneration than activated carbon. Although the price of doped K−OMS-2 is higher than activated carbon, the total operation cost of doped K−OMS-2 can be compensated by its capacity and longevity. The catalysts tested here indicate that doped K−OMS-2 has potential application in the removal of aqueous phenol from the synthetic fuel and other industries.

**Acknowledgment.** This project was funded by the Chemical Sciences, Geosciences, and Biosciences Division of the Office of Basic Energy Sciences, and Office of Science, U.S. Department of Energy. We thank Dr. Frank Galasso for helpful discussions and Dr. Abhay Vaze for help with the AA analysis.

**Supporting Information Available:** Supporting Figures S1−S3. This material is available free of charge via the Internet at http://pubs.acs.org.

## References and Notes

(1) Kumar, R.; Sithambaram, S.; Suib, S. L. Cyclohexane Oxidation Catalyzed by Manganese Oxide Octahedral Molecular Sieves−Effect of Acidity of the Catalyst. *J. Catal.* **2009**, *262*, 304–313.

(2) Zhang, L.; Liu, C.; Zhuang, L.; Li, W.; Zhou, S.; Zhang, J. Manganese Dioxide as an Alternative Cathodic Catalyst to Platinum in Microbial Fuel Cells. *J. Biosens. Bioelectron.* **2009**, *24*, 2825–2829.

(3) Yuan, J.; Liu, X.; Akbulut, O.; Hu, J.; Suib, S. L.; Kong, J.; Stellacci, F. Superwetting Nanowire Membranes for Selective Absorption. *Nat. Nanotechnol.* **2008**, *3*, 332–336.

(4) Resini, C.; Catania, F.; Berardinelli, S.; Paladino, O.; Busca, G. Catalytic Wet Oxidation of Phenol over Lanthanum Strontium Manganite. *Appl. Catal., B* **2008**, *84*, 678–683.

(5) Arena, F.; Negro, J.; Parmaliana, A.; Spadaro, L.; Trunfio, G. Improved MnCeO*x* Systems for the Catalytic Wet Oxidation (CWO) of Phenol in Wastewater Streams. *Ind. Eng. Chem. Res.* **2007**, *46*, 6724–6731.

(6) Nayak, P. S.; Singh, B. K. Removal of Phenol from Aqueous Solutions by Sorption on Low Cost Clay. *Desalination* **2007**, *207*, 91–79.

(7) Duprez, D.; Delanoe, F.; Barbier, J., Jr.; Isnard, P.; Blanchard, G. Catalytic Oxidation of Organic Compounds in Aqueous Media. *Catal. Today* **1996**, *29*, 317–322.

(8) Polverejan, M.; Villegas, V. C.; Suib, S. L. Higher Valency Ion Substitution into the Manganese Oxide Framework. *J. Am. Chem. Soc.* **2004**, *126*, 7774–7775.

(9) Calvert, C.; Joesten, R.; Ngala, K.; Villegas, J.; Morey, A.; Shen, X.; Suib, S. L. Synthesis, Characterization, and Rietveld Refinement of Tungsten-Framework-Doped Porous Manganese Oxide (K-OMS-2) Material. *Chem. Mater.* **2008**, *20*, 6382–6388.

(10) Teruhito, S.; Shinichi, K.; Naoaki, K.; Izumi, N. Synthesis of Hollandite-Type $K_y(Mn_{1-x}M_x)O_2$ (M = Co, Fe) by Oxidation of Mn(II) Precursor and Preliminary Results on Electrode Characteristics in Rechargeable Lithium Batteries. *Electrochem. Solid-State Lett.* **2005**, *8*, 471–475.

(11) Luo, J.; Zhu, H. T.; Fan, H. M.; Liang, J. K.; Shi, H. L.; Rao, G. H.; Li, J. B.; Du, Z. M.; Shen, Z. X. Synthesis of Single-Crystal Tetragonal α-$MnO_2$ Nanotubes. *J. Phys. Chem. C* **2008**, *112*, 12594–12598.

(12) Xu, M.; Kong, L.; Zhou, W.; Li, H. Hydrothermal Synthesis and Pseudocapacitance Properties of α-$MnO_2$ Hollow Spheres and Hollow Urchins. *J. Phys. Chem. C* **2007**, *111*, 19141–19147.

(13) Edward, K. N.; Chen, C.; Sithambaram, S.; Crisostomo, V. B.; Suib, S. L. Systematic Control of Particle Size in Rapid Open-Vessel Microwave Synthesis of K-OMS-2 Nanofibers. *J. Phys. Chem. C* **2008**, *112*, 6786–6793.

(14) Luo, J.; Zhang, Q.; Huang, A.; Suib, S. L. Total Oxidation of Volatile Organic Compounds with Hydrophobic Cryptomelane-type Octahedral Molecular Sieves. *Microporous Mesoporous Mater.* **2000**, *209*, 35–36.

(15) Xu, R.; Wang, X.; Wang, D.; Zhou, K.; Li, Y. Surface Structure Effects in Nanocrystal $MnO_2$ and Ag/$MnO_2$ Catalytic Oxidation of CO. *J. Catal.* **2006**, *237*, 426–430.

(16) Sriskandakumar, T.; Opembe, N.; Chen, C.; Morey, A.; King'ondu, C.; Suib, S. L. Green Decomposition of Organic Dyes Using Octahedral Molecular Sieve Manganese Oxide Catalysts. *J. Phys. Chem. A* **2009**, *113*, 1523–1530.

(17) Koitaya, T.; Nakamura, H.; Yamashita, K. First-Principle Calculations of Solvated Electrons at Protic Solvent-$TiO_2$ Interfaces with Oxygen Vacancies. *J. Phys. Chem. C* **2009**, *113*, 7236–7245.

(18) Jiang, H. L.; Tay, J. H.; Tay, S. T. L. Changes in Structure, Activity and Metabolism of Aerobic Granules as a Microbial Response to High Phenol Loading. *Appl. Microbiol. Biotechnol.* **2004**, *63*, 602–608.

(19) Polaert, I.; Wilhelm, A. M.; Delmas, H. Phenol Wastewater Treatment by a Two-step Adsorption-Oxidation Process on Activated Carbon. *Chem. Eng. Sci.* **2002**, *57*, 1685–1590.

(20) Yuan, J.; Laubernds, K.; Villegas, J.; Gomez, S.; Suib, S. L. Spontaneous Formation of Inorganic Paper-like Materials. *Adv. Mater.* **2004**, *16*, 1729–1732.

(21) Cullity, B. D.; Stock, S. R. *Elements of X-Ray Diffraction*, 3rd ed.; Prentice-Hall: Upper Saddle River, NJ, 2001.

(22) Abecassis-Wolfovich, M.; Jothiramalingam, R.; Landau, M. V.; Herskowitz, M.; Viswanathan, B.; Varadarajan, T. K. Cerium Incorporated Ordered Manganese Oxide OMS-2 Materials: Improved Catalysts for Wet Oxidation of Phenol Compounds. *Appl. Catal., B* **2005**, *59*, 91–98.

(23) Krasil'nikova, O. K.; Kazbanov, N. S.; Gur'yanov, V. V. Effect of Temperature on Adsorption of Phenol on Microporous Activated FAS-Type Carbons. *Prot. Met. Phys. Chem. Surf.* **2009**, *45*, 518–524.

(24) Santos, A.; Yustos, P.; Quintanilla, A.; Garcia-Ochoa, F.; Casas, J. A.; Rodriguez, J. Evolution of Toxicity upon Wet Catalytic Oxidation of Phenol. *J. Environ. Sci. Technol.* **2004**, *38*, 133–138.

(25) Topping, D. C.; Bernard, L. G.; O'Donoghue, J. L.; English, J. C. Hydroquinone: Acute and Subchronic Toxicity Studies with Emphasis on Neurobehavioral and Nephrotoxic Effects. *Food Chem. Toxicol.* **2007**, *45*, 70–78.

(26) Gao, T.; Glerup, M.; Krumeich, F.; Nesper, R.; Fjellvag, H.; Norby, P. Microstructures and Spectroscopic Properties of Cryptomelane-type Manganese Dioxide Nanofibers. *J. Phys. Chem. C* **2008**, *112*, 13134–13140.

(27) Aktas, N.; Sahiner, N.; Kantoglu, O.; Salih, B.; Tanyola, A. Biosynthesis and Characterization of Laccase Catalyzed Poly(Catechol). *J. Polym. Environ.* **2003**, *11*, 123–128.

(28) Shen, Y. F.; Suib, S. L.; O'Young, C. L. Characterization of Manganese Oxide Octahedral Molecular Sieve (M-OMS-2) Materials with Different Cation Dopants. *Chem. Mater.* **2002**, *14*, 940–948.

(29) Stuber, F.; Font, J.; Fortuny, A.; Bengoa, C.; Eftaxias, A.; Fabregat, A. Carbon Materials and Catalytic Wet Air Oxidation of Organic Pollutants in Wastewater. *Top. Catal.* **2005**, *33*, 3–50.

(30) Shannon, R. D. Revised Effective Ionic Radii and Systematic Studies of Interatomic Distances in Halides and Chalcogenides. *Acta Crystallogr.* **1976**, *32*, 751–767.

(31) Feng, Q.; Kanoh, H.; Miyai, Y.; Ooi, K. Alkali Metal Ions Insertion/Extraction Reactions with Hollandite-Type Manganese Oxide in the Aqueous Phase. *Chem. Mater.* **1995**, *7*, 148–153.

(32) Tamura, H.; Mita, K.; Tanaka, A.; Ito, M. Mechanism of Hydroxylation of Metal Oxide Surfaces. *J. Colloid Interface Sci.* **2001**, *243*, 202–207.

(33) Gilbert, B. C.; Kamp, W. J. N.; Smith, R. L. J.; Oakes, J. EPR Evidence for One-electron Oxidation of Phenols by a Dimeric Manganese(IV/IV) Triazacyclononane Complex in the Presence and Absence of Hydrogen Peroxide. *J. Chem. Soc., Perkin Trans.* **1997**, *2*, 2161–2165.

(34) Gopalan, S.; Savage, E. P. Reaction Mechanism for Phenol Oxidation in Supercritical Water. *J. Phys. Chem.* **1994**, *98*, 12646–12652.

(35) Makwana, V. D.; Son, Y. C.; Howell, A. R.; Suib, S. L. The Role of Lattice Oxygen in Selective Benzyl Alcohol Oxidation Using OMS-2 Catalyst: A Kinetic and Isotope-Labeling Study. *J. Catal.* **2002**, *210*, 46–52.

(36) Tiemann, K. J.; Gardea-Torresdey, J. L.; Gamez, G.; Dokken, K.; Cano-Aguilera, I.; Renner, M. W.; Furenlid, L. R. Effects of Oxidation State on Metal Ion Binding by *Medicago sativa* (Alfalfa): Atomic and X-ray Absorption Spectroscopic Studies with Fe(II) and Fe(III). *Environ. Sci. Technol.* **2000**, *34*, 693–698.

(37) Stone, A. T. Reductive Dissolution of Manganese (III/Iv) Oxides by Substituted Phenols. *Environ. Sci. Technol.* **1987**, *21*, 979–988.

(38) Chaires, J. B. Calorimetry and Thermodynamics in Drug Design. *Annu. Rev. Biophys.* **2008**, *37*, 135–151.

(39) Suib, S. L. Structure, Porosity, and Redox in Porous Manganese Oxide Octahedral Layer and Molecular Sieve Materials. *J. Mater. Chem.* **2008**, *18*, 1623–1631.

(40) Li, X.; Hu, B.; Suib, S.; Lei, Y.; Li, B. Manganese Dioxide as a New Cathode Catalyst in Microbial Fuel Cells. *J. Power Sources* **2010**, *195*, 2586–2591.

(41) Yin, Y.; Xu, W.; DeGuzman, R.; Suib, S. L.; O'Young, C. L. Studies of Stability and Reactivity of Synthetic Cryptomelane-like Manganese Oxide Octahedral Molecular Sieves. *Inorg. Chem.* **1994**, *33*, 4384–4389.

(42) Dabrowski, A.; Podkoscielny, P.; Hubicki, Z.; Barczak, M. Adsorption of Phenolic Compounds by Activated Carbon−a Critical Review. *Chemosphere* **2005**, *58*, 1049–1070.

JP100819A